

Automated Visual Inspection of Glass Bottle Bottom With Saliency Detection and Template Matching

Xianen Zhou^{ID}, Yaonan Wang, Changyan Xiao^{ID}, Qing Zhu^{ID}, Xiao Lu, Hui Zhang, Ji Ge, and Huihuang Zhao

Abstract—Glass bottles are widely used as containers in the food and beverage industry, especially for beer and carbonated beverages. As the key part of a glass bottle, the bottle bottom and its quality are closely related to product safety. Therefore, the bottle bottom must be inspected before the bottle is used for packaging. In this paper, an apparatus based on machine vision is designed for real-time bottle bottom inspection, and a framework for the defect detection mainly using saliency detection and template matching is presented. Following a brief description of the apparatus, our emphasis is on the image analysis. First, we locate the bottom by combining Hough circle detection with the size prior, and we divide the region of interest into three measurement regions: central panel region, annular panel region, and annular texture region. Then, a saliency detection method is proposed for finding defective areas inside the central panel region. A multiscale filtering method is adopted to search for defects in the annular panel region. For the annular texture region, we combine template matching with multiscale filtering to detect defects. Finally, the defect detection results of the three measurement regions are fused to distinguish the quality of the tested bottle bottom. The proposed defect detection framework is evaluated on bottle bottom images acquired by our designed apparatus. The experimental results demonstrate that the proposed methods achieve the best performance in comparison with many conventional methods.

Index Terms—Defect detection, machine vision, multiscale filtering, saliency detection, template matching.

I. INTRODUCTION

G LASS bottles are widely used as containers in the food and beverage industry, especially for beer and carbon-

Manuscript received July 10, 2018; revised October 7, 2018; accepted November 26, 2018. This work was supported in part by the National Science Foundation of China under Grant 61733004, Grant 61703155, Grant 61573134, and Grant 61503128, in part by the Hunan Key Project of Research and Development Plan under Grant 2017XK2102, Grant 2018GK2022, and Grant 2018JJ3079, and in part by the Innovation Project of Postgraduate Student in Hunan Province of China under Grant CX2017B108. The Associate Editor coordinating the review process was Emanuele Zappa. (*Corresponding authors: Changyan Xiao; Qing Zhu.*)

X. Zhou, Y. Wang, C. Xiao, and Q. Zhu are with the National Engineering Laboratory for Robot Visual Perception and Control Technology, College of Electrical and Information Engineering, Hunan University, Changsha 410082, China (e-mail: c.xiao@hnu.edu.cn; zhuqing_hnu@163.com).

X. Lu is with the College of Engineering and Design, Hunan Normal University, Changsha 410081, China.

H. Zhang is with the College of Electrical and Information Engineering, Changsha University of Science and Technology, Changsha 410114, China.

J. Ge is with the Advanced Micro and Nanosystems Laboratory, University of Toronto, Toronto, ON M5S 3G8, Canada.

H. Zhao is with the College of Computer Science and Technology, Hengyang Normal University, Hengyang 421008, China.

Color versions of one or more of the figures in this paper are available online at <http://ieeexplore.ieee.org>.

Digital Object Identifier 10.1109/TIM.2018.2886977

ated beverages [1], because glass bottles are easy to mold, easy to recycle, relatively inexpensive, and highly resistant to internal pressure [2]. However, glass bottles can also be easily damaged in the transport process and in various manufacturing processes. In addition, smudges and foreign material may exist on the bottle surface, especially on reused bottles [3]. The bottle bottom is a key part of a glass bottle. If a bottle that possesses bottom defects is filled, potential hazards may occur during product storage and transportation. Hence, the quality of the bottle bottom must be strictly checked before filling the bottle.

The conventional bottle bottom inspection methods rely on manual inspection, and they suffer from inherent inconsistency and unreliability because the entire inspection process is subjective and very tedious [4], [5]. As a promising and nondestructive measurement technique, machine vision-based defect detection has been widely applied in medicine [6], [7], food [8], beverage [4], and many other fields [9]–[17]. This approach also provides a flexible solution to bottle bottom quality control. To date, even though many patents related to bottle bottom inspection devices have been filed [3], [18], [19] and there exist several commercial vision systems available for bottle inspections [20], [21]. However, there are still many problems to be solved, such as the inaccurate localization of bottle bottom, the difficulty in defect detection of texture region, and the interference of gray-value variety across the central panel. Some directly related papers are also discussed. Shafait *et al.* [22] presented a simple method. They first locate the center of the bottle bottom with a generalized Hough transform. Then, they check each gray value in the region of interest (ROI) to distinguish defective regions. If the intensity of an individual pixel does not lie within the tolerance limit, then the pixel is designated as an outlier. Otherwise, the pixel is labeled as normal. This is a simple and fast method because it depends on only two thresholds. However, the result is susceptible to the impact of many factors, such as light intensity inhomogeneity and bottom thickness variety. To enhance the robustness, Duan *et al.* [4] introduced a defect detection approach based on a back propagation neural network for the bottle bottom and bottle body. The 6-D features, including the gradient and many binary values obtained by thresholds, are first calculated. Then, two artificial neural networks are used for low-level inspection and high-level judgment. The structure of the network is complicated. Therefore, training the network is time-consuming. To accelerate the process, Ma *et al.* [23] and Huang *et al.* [24] employed least squares circle detection

and redefined randomized circle detection algorithms to locate the ROI of the bottle bottom, and they applied the blob algorithm and discrete Fourier transform (DFT) to detect defects in the panel and texture regions, respectively [25]. However, there is no further discussion regarding how to obtain blobs. Consider that global thresholding segmentation (GTS) and adaptive thresholding segmentation (ATS) are two simple and popular methods to obtain blobs, they will be discussed in the comparison experiments in this paper. All these traditional methods have some common problems. For example, when glass chips and transparent foreign particles are present on the bottle bottom, the thicknesses of the bottle bottoms are different, or foreign materials and contaminants exist in the texture region. Precisely detecting defects are difficult.

To find a suitable solution for bottle bottom inspection, many similar works in surface defect detection problems are further analyzed. Liu *et al.* [1] combined a support vector machine with fuzzy theory to inspect defects of the bottle body. In [26], a simple method of thresholding and edge extracting was used to detect defects on mouths of vials. Zhou *et al.* [27] used a fast sparse-representation-based detection algorithm to detect surface defects on bottle caps. A wavelet-based method was used for defect detection in [28]–[30]. Many anisotropic diffusion model (AD)-based methods [31]–[35] are also widely used for surface defect detection, especially for low-contrast images. Superpixel segmentation and a bi-Gaussian filter were fused to extract defects on the inner surface of can ends [4]. Saliency detection methods are also a good choice for object detection and surface defect detection [36]–[38]. Moreover, the active contour model [39], [40], Gabor filtering [41], [42], and the expectation-maximization technique [43] could also be used for surface defect detection. Although there are many surface defect detection algorithms, they were mostly developed to solve specific problems. Hence, only few of these algorithms can be directly applied to bottle bottom inspection.

In this paper, we present an automated visual apparatus, and we propose a framework using the saliency detection and template matching for bottle bottom inspection with real-time speed. The emphasis is placed on image processing algorithms for defect detection across different bottle bottom regions. The main contribution of this paper is fourfold.

- 1) An automated visual detection system is designed to detect defects for bottle bottoms.
- 2) A defect detection framework with saliency detection and template matching for glass bottle bottoms is proposed. The proposed framework consists of three parts, which are applied to detect defects in the central panel, annular panel, and annular texture region of glass bottle bottoms.
- 3) We propose saliency detection algorithms that include a redefined geodesic saliency detection and a 1-D saliency detection based on multiscale mean filtering used for defect detection in panel regions of bottle bottoms. These methods can improve the robustness of defect detection by raising the contrast between the background area and all suspected defects.

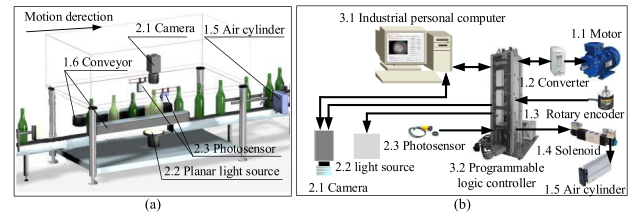


Fig. 1. System structure and electrical control system of the developed apparatus. (a) System structure. (b) Electrical control system.

- 4) We propose an annular texture region defect detection method composed of template matching and multiscale mean filtering, which can improve the robustness to gray-value variety.

This paper is organized as follows. The system architecture, imaging system, and defects and challenges are introduced in Section II. Section III illustrates the proposed defect detection framework for glass bottle bottoms. The experimental results are presented in Section IV. Finally, Section V presents the conclusion.

II. SYSTEM DESIGN

In this section, the system architecture of the glass bottle bottom inspection apparatus is first introduced, and particular considerations regarding the illumination scheme are presented. Then, the image properties and the challenges for defect detection are investigated.

A. System Architecture

The system structure and electrical control system are illustrated in Fig. 1. The apparatus mainly consists of three components: 1) an electromechanical device; 2) an imaging system; and 3) a processing module. Among these components, the electromechanical device is composed of motors (1.1), converters (1.2), an encoder (1.3), and so on. This component is used to achieve automatic motion control and sorting of bottles. The imaging system, which consists of a camera (2.1), light source (2.2), and photosensor (2.3), is designed to acquire high-quality images for the fast-moving test items. The processing module is composed of a computer (3.1) and programmable logic controller (PLC) (3.2). This module is adopted to process the obtained image and control the operation of the machine. The glass bottle is grabbed by both conveyor belts (1.6), as shown in Fig. 1(a). When it is transmitted to the photoelectric sensor (2.3), a trigger signal is generated, and this signal is received by the PLC (3.2). Then, the PLC generates two signals to turn on the planar light source (2.2) immediately and to trigger the camera (2.1), which captures a bottom image. Finally, the computer (3.1) implements the proposed defect detection framework and outputs the results. If any defect of a bottle bottom is detected, the bottle is considered as defective, which is not approved by the visual inspection system. In other words, the defective bottle will be removed from the production line by an air cylinder (1.5).

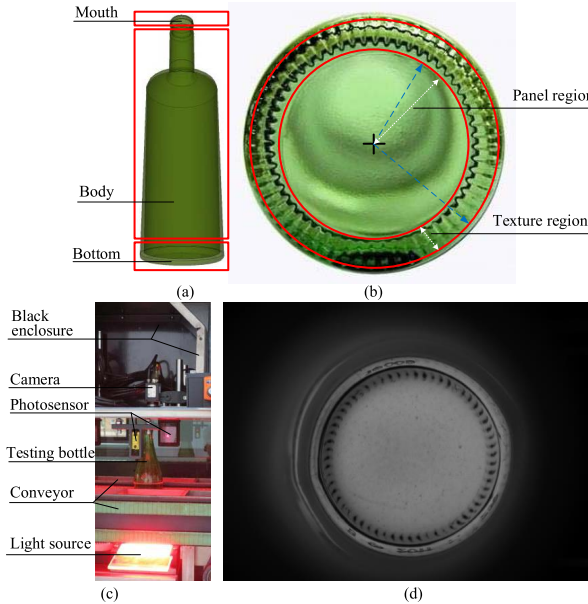


Fig. 2. Demonstrate the structure of a glass bottle and our designed imaging system. (a) Bottle. (b) Bottom. (c) Real imaging system. (d) Real bottom image.

B. Imaging System

The glass bottle is usually composed of three parts including bottom, body, and mouth, as shown in Fig. 2(a). The bottle bottom consists of two parts: a texture region and a panel region, as shown in Fig. 2(b). We focus on defect detection in the central panel region and annular region of the bottle bottom. To capture an image that can display these abnormal regions clearly, we designed the imaging system composed of a camera and a planar light source, as shown in Fig. 2(c). The camera, which is installed in a closed box, in which the inner surface is painted black in order to avoid ambient light interference, is situated above the bottle and looks down at the bottle bottom through the neck opening of the bottle. The bottom is, in turn, illuminated from below by a planar light source, which is sufficiently large to illuminate the entire bottom. The limiting camera resolution, I_{LCR} , is calculated by $I_{LCR} = (S_{FOV}/S_{MD}) * N_{PD}$, where S_{FOV} and S_{MD} denote the sizes of the field of view (FOV) and minimal defect, respectively. The minimal defect requires at least N_{PD} pixels to represent. In this paper, $S_{FOV} \approx 120$ mm, $S_{MD} = 1$ mm, $N_{PD} = 4$. Hence, the minimum resolution meeting our requirement is 480×480 . A camera with a resolution of 648×483 is sufficient to satisfy the inspection requirement. The real image from the in-field inspection is acquired in a grayscale format, as shown in Fig. 2(d).

C. Defects and Challenges

As shown in Fig. 2(d), in an ideal situation, images of the normal bottle bottoms generally have relatively uniform gray levels in each region. However, due to different thicknesses of bottle bottoms, the image of a normal bottle bottom also has irregular gray levels. In addition, the bottle bottom inspection is considered to be particularly difficult due to many other

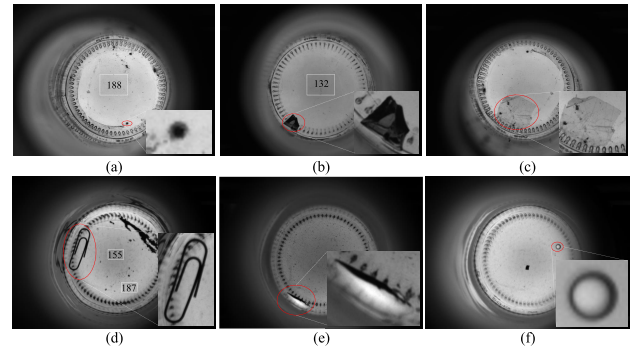


Fig. 3. Typical defects of bottle bottoms with (a) smudginess, (b) glass detritus, (c) transparent film, (d) paperclip, (e) damaged bottom, and (f) bubble. Here, the red ellipse marked regions are magnified and displayed at the lower right corner of each subfigure, and the digits represent the mean gray values of the white rectangular regions.

complex factors. Here, beer bottles are used for demonstration. After the beer inside the bottle has been consumed, there are cases where cigarette butts, transparent films, bottle caps, paperclips, and so forth are pressed into the bottle; additionally, foreign particles including glass chips due to bottle mouth cracks enter the bottle [3]. Such foreign particles, including glass detritus, transparent film, paperclips, and many varieties of materials, have different types of optical characteristics to such an extent that it is extremely difficult to detect all of these objects simultaneously. Moreover, the bottle bottom is susceptible to damage during transportation and processing.

To further understand the complexity of bottle bottom inspection, we divide bottle bottom flaws into four different types according to the reflected features in the obtained images.

- 1) *Opaque Foreign Objects*: The gray level of opaque foreign objects in the bottle bottom image is clearly lower than that of the normal region. In addition, the edges of the opaque foreign objects are very clear and sharp. Take the large glass detritus and the paperclip as examples, as shown in Fig. 3(b) and (d).
- 2) *Transparent Foreign Objects*: The region corresponding to transparent foreign objects in the bottle bottom image is similar to the normal region. The edges are not sharp. Take the transparent film as an example, as shown in Fig. 3(c).
- 3) *Contaminants*: As shown in Fig. 3(a), the gray level of the contaminant region is typically lower than that of the normal region. In addition, the differences in boundary region are not very large.
- 4) *Self-Defects*: Their marginal region is generally smooth. The gray feature of the obtained image is in complete contrast to that of the contaminant. Take the broken glass and bubble as examples, as shown in Fig. 3(e) and (f).

From the previous analysis, the main challenges in detecting bottle bottom defects can be summarized as follows.

- 1) The gray values of the panel region change in a great range for different bottle bottom images, even though these images are obtained by the same system with the same parameter settings, and the corresponding tested

bottles are also the same type of glass bottle. The problem may also be caused by the thicknesses of different bottoms being different. For example, the average gray value of the white rectangular region in Fig. 3(a) is 188, while that of the region in Fig. 3(b) is 132. Specifically, even for the same bottom image, the grayscale distribution may vary remarkably in different locations, as shown in Fig. 3(d).

- 2) The contrast between the defective region and the normal region is very low; for instance, when a transparent film exists on the bottom, the corresponding captured image is shown in Fig. 3(c). The grayscale values of defects are very different. When the bottom has been broken, the grayscale values of the broken region are larger than those of the background, as shown in Fig. 3(e). When smudges, paperclips, transparent film, and other foreign materials exist on the bottom, the gray values of the defective regions are smaller than those of the normal region, as shown in Fig. 3(a)–(d).
- 3) The category of defects, the scale of defects, and the position of defects are diverse.
- 4) Defects, particularly small and low-contrast defects, existing in the texture region are difficult to detect because the texture size, shape, and grayscale level may also change sharply.

III. BOTTLE BOTTOM INSPECTION METHOD

To overcome the problems described earlier, we proposed an image analysis pipeline for glass bottle bottom inspection according to the features of defects. As shown in Fig. 4, the bottom is first located through a Hough transform circle detection. Then, the bottom is divided into the central panel region and annular region, the latter is further segmented into two subregions: the annular panel region and the annular texture region. In the following, three different algorithms are applied to detect defects in different regions, where defect detection methods based on a geodesic distance transform and multiscale filtering are proposed for inspecting defects in the center panel region and the annular panel region, respectively. A defect detection method based on template matching is proposed for detecting defects in the annular texture region. Finally, the inspection results of the three regions are fused to distinguish the quality of the entire bottle bottom, as well as to display a complete result of defect detection. The consumed time of our entire framework is approximately 133 ms when the framework is executed on a computer configured with an Intel(R) Core(TM) i5-4210U (1.7–2.4 GHz) and 6 GB of memory. The consumed time of each process and the corresponding proportion of total time consumption are also given in Fig. 4. Defect detection with our framework on nine tested bottle bottom is given in Fig. 5. It is clear that the majority of typical defects can be correctly detected. By changing the parameter settings, the proposed framework is applicable to a diversity of bottle bottom samples with various colors and sizes. However, the shape of the bottom of the tested bottle must be cylindrical since the ROI of the bottle bottom image is obtained by the Hough circle detection. The schematic of a tested bottle model is given in Fig. 2(a).

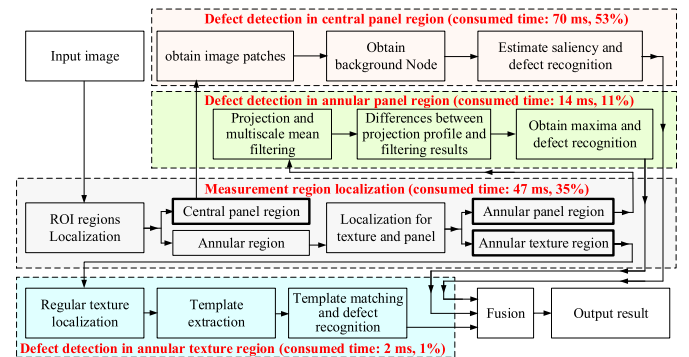


Fig. 4. Proposed defect detection framework.

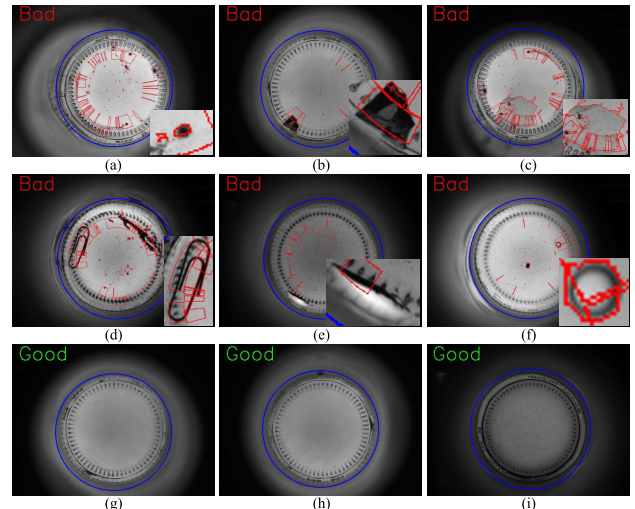


Fig. 5. Defect detection with the proposed framework. (a)–(i) Defect detection results for typical glass bottle bottoms. Here, the detection results are marked with rectangles in the lower right corner of (a)–(f) corresponding to the typical defects in Fig. 3. The red “Bad” and green “Good” in the upper left corner of each figure, respectively, indicate the unqualified and qualified bottle bottoms.

A. Measurement Region Localization

Due to mechanical vibration from conveyor motion and random errors of the software system, the ROI of the bottle does not present at a fixed position in the obtained images. Therefore, it is necessary to locate the object beforehand.

In this paper, we combine circle detection with size priors to obtain the ROI because the bottle bottom is a standard circular object and has a fixed size for a certain type of bottle. We use the 2HT algorithm [44], which consists of two steps, radius detection and center detection, to obtain the ROI of the bottom. 2HT, which requires less memory and has higher efficacy than the traditional Hough circle detection method [45], is one of the most popular circle detection methods and has been implemented in many popular image processing tools, such as OpenCV and MATLAB. After localization, the input image is divided into two measurement regions, namely, the central panel region and annular region, as shown in Fig. 6(b) and (c), the latter is defined by its inner radius R_{a_min} and outer radius R_{a_max} . The radius of the central panel region is R_c . R_{a_min} , R_{a_max} , and R_c are set according to prior knowledge

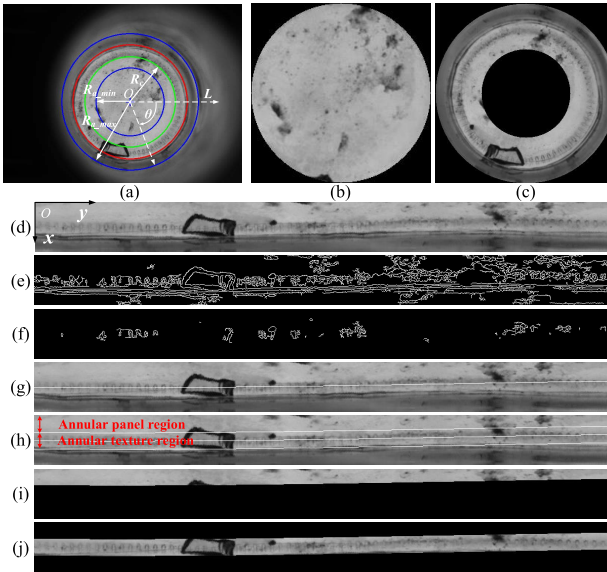


Fig. 6. Measurement region localization. (a) Glass bottle bottom location. The red circle is the region obtained by the proposed localization method. The region in the green circle is the central panel region. The region between the large blue circle and the small blue circle is the annular region. (b) Enlarged figure of the central panel region. (c) Enlarged figure of the original annular region. (d) Annular region unwrapping. (e) Canny edges. (f) Edges that belong to the texture region. (g) Central line of the annular texture region obtained by polynomial fitting. (h) Annular panel and texture regions obtained by the size prior of the regular texture. (i) Annular panel region. (j) Annular texture region.

of the bottle bottom. To ensure reliability for defect detection, we reserve a common panel region for the central panel region and annular region, as shown in Fig. 6(a), which is between the green circle and the small blue circle. The annular region is a ring-shaped image, which is inconvenient for the follow-up image processing. Thus, we transform it into a rectangular image with the radial development approach [8] in polar coordinates with pole O and polar axis L denoted by the white dotted line in Fig. 6(a), where the polar angle θ is measured clockwise from the axis L . Followed, the annular region unwrapping image, as shown in Fig. 6(d), named as the annular region, is further divided into two subparts, namely, annular panel region and annular texture region, and the corresponding flowchart is presented in Fig. 6(d)–(j). It is mainly composed of three steps: edge extraction, denoising, and polynomial fitting. The rectangular image obtained by the radial development approach is first fed into the Canny algorithm to abstract edges since each texture generally has a sharp boundary. Then, the interference connected edges are searched and removed according to two features: the length of the connected edge denoted by F_{LCE} , and the ratio of the height to width denoted by F_{RHW} . If F_{LCE} and F_{RHW} of an edge are too large or too small, the edge is considered as an interference edge and removed. Finally, the remaining edges are taken as the input data, and we use a polynomial of degree three to fit the input data, which is similar to [46]. p_1 , p_2 , p_3 , and p_4 are four coefficients of the polynomial $x = f(y)$, which is given as

$$f(y) = p_1 + p_2y + p_3y^2 + p_4y^3. \quad (1)$$

Depending on the x -coordinates and the y -coordinate of the input data, four coefficients can be obtained with the least squares method. In other words, the central line of all regular texture regions, i.e., $f(y)$, is obtained, as shown by the white line in Fig. 6(g). Finally, we combine the height prior of the texture region with the central line to obtain the annular texture region and annular panel region, as shown in Fig. 6(i) and (j). We realign the annular texture region by the polynomial fitting without a requirement of $f(0^\circ) = f(360^\circ)$. Because the main purpose of the fitting is to divide the annular region into two subregions: annular panel region and annular texture region. Moreover, the fitted result usually has little effect on the final defect detection result since the majority of interference edges have been removed.

B. Defect Detection in Annular Texture Region

Defects in the annular region are diverse. Moreover, the complex structures of the bottle bottom make the gray-level distribution vary remarkably with changing location. These factors dramatically increase the difficulty of defect detection. Fortunately, in the same bottom image, the majority of texture regions are usually similar to each other in shape and size. Hence, we propose a template-matching-based defect detection algorithm named TM for short, as shown in Fig. 7, which includes three steps: regular texture localization, template extraction, and template matching and defect recognition.

1) Regular Texture Localization: Regular texture localization consists of three subparts: gray projection, mean filtering, and ridge detection, as shown in Fig. 7(a)–(c). First, the projection profile of the ROI strip is obtained by accumulating the gray levels in the x -coordinate direction. However, the obtained 1-D signal is very noisy, as shown in Fig. 7(b). To reduce noise, mean filtering is used for smoothing the projection profile. Ridges generally appear on the central line between the two adjacent texture regions. On this basis, we can locate each regular texture region by detecting ridges in the y -coordinate direction. Finally, we search all local peaks of the obtained 1-D signal, and beginning from the first peak, we remove those peaks separated by less than a distance threshold, which is set manually according to the width prior of the texture region. The remaining ridges are the final ridge detection result, as shown in 7(c).

2) Template Extraction: For different bottle bottoms, although these bottles belong to the same type, the differences in regular texture are particularly great because the used time is inconsistent for recycled bottles. Thus, we must extract the corresponding template of regular texture for each tested bottle bottom.

The flowchart of template extraction is presented in Fig. 7(d)–(g). First, we transform the curvilinear strip into a regular rectangular image to facilitate the follow-up process of image processing, as shown in Fig. 7(d). Then, the width of each texture region and the appearance frequency of each width are computed. Finally, we obtain the regular texture regions with the maximum frequency and take the average gray levels of all obtained texture regions as the template, as shown in 7(g), because the defective regions cover only the minority of the whole annular region, and their appearance

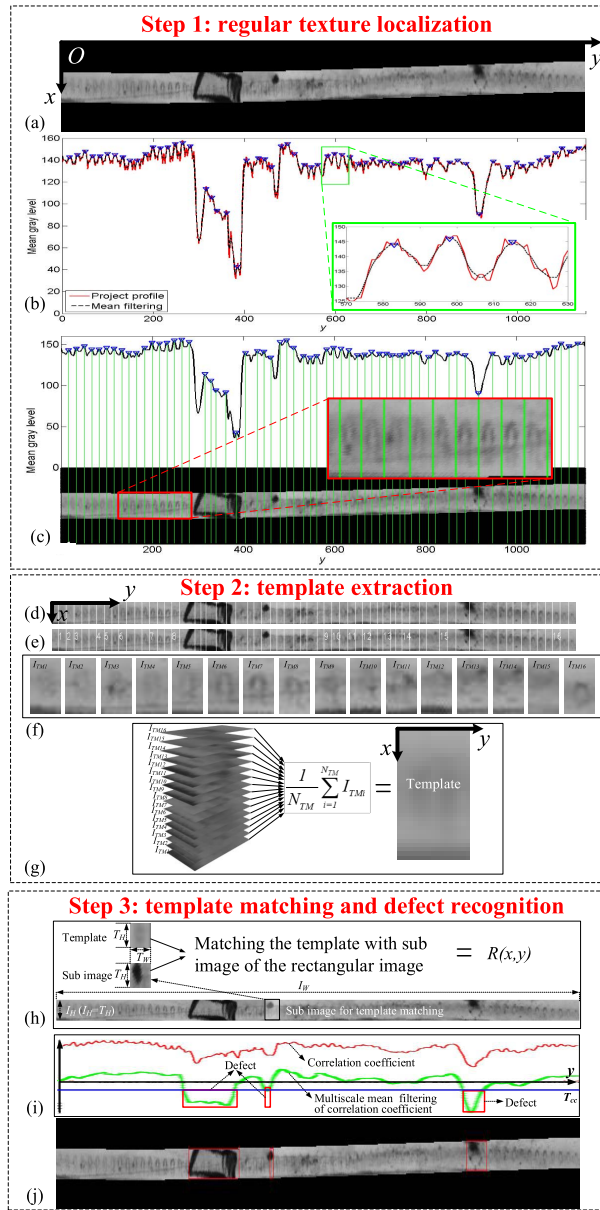


Fig. 7. Process of detecting defects in the annular texture region. (a) Annular texture region. (b) Projection profile, the corresponding mean filtering and the local maximum of the mean filtering signal. The location of the local maximum of the mean filtering projection profile is marked by the blue “ ∇ .” (c) y-coordinate localization of each regular texture. The green line denotes the location of the local maximum of the mean filtering projection profile, which is generally the y-coordinate central line of both adjacent regular textures. (d) Rectangular image of the annular texture region. (e) Texture regions used for generating the template of the texture region. The objective regular texture regions are marked by the white numbers. (f) Enlarged figures of the objective textures for generating the template. (g) Average template of the texture region. (h) Rectangular image of annular texture region and template matching. (i) Correlation coefficient and the multiscale filtering result. (j) Defect detection result in the annular texture region.

frequency is typically very low. Consider that the template is the average appearance of many defect-free texture regions, it is named average template, which always takes the same size as the matched subimage in the rectangular image during matching or correlation measurement.

3) *Template Matching and Defect Recognition*: The overall process of template matching and defect recognition is

illustrated in Fig. 7(h)–(j). First, the correlation coefficient denoted by $R(x, y)$, as shown by the red curve in Fig. 7(i), between the average template and the rectangular image is calculated from the equation (2): where T_W and T_H , respectively, represent the width and the height of the average template. I_W and I_H are the width and the height of the rectangular image, $I_H = T_H$. $I_{AT}(x, y)$ and $T(i, j)$ denote a pixel in the rectangular and template images, respectively. The coordinates of the former are x and y , and those of the latter are i and j . \bar{T} and $\bar{I}_{AT}(x, y)$ are the average values of the template and subimage of the rectangular image, where the coordinates of the center of the latter are x and y . Both of them are given as

$$\bar{T} = \frac{1}{T_H T_W} \sum_{i=1}^{T_H} \sum_{j=1}^{T_W} T(i, j) \quad (3)$$

$$\bar{I}_{AT}(x, y) = \frac{1}{T_H T_W} \sum_{i=1}^{T_H} \sum_{j=1}^{T_W} I_{AT}(x + i, y + j) \quad (4)$$

where x and y in (2), as shown at the bottom of the next page and (4) are a constant and a variable, respectively, $x = (I_H + 1)/2$, and $y \in [(T_W - 1)/2, I_W - T_W + 1]$. The process of template matching is similar to a kernel filter. The difference is that the template slides only along the central line of the rectangular image. As shown in Fig. 7(h) and (i), a defect generally appears as a valley on the corresponding correlation coefficient signal. However, the local variation caused by defects on the correlation coefficient curve may not be obvious and may contain noise. Hence, $R(x, y)$ is fed into an approach, which combines a multiscale mean filtering algorithm with the traditional valley detection method [47] to further highlight defective areas. For the multiscale mean filtering algorithm, the 1-D correlation coefficient signal is first filtered by mean filtering with different scales of filtering masks. Then, the maximum response under all scales is taken as the final filtering output. After this process, defects generally appear as the obvious valleys on the filtered signal, as shown by the green curve in Fig. 7(i). Finally, a threshold T_{cc} , as shown by the blue line in Fig. 7(i), is adopted to discriminate desired defects from noisy interference. The parts whose values are lower than T_{cc} are considered as the real defective segments, as shown in Fig. 7(j).

C. Defect Detection in Annular Panel Region

In Fig. 8, the full flowchart of defect detection for the annular panel region is presented. The proposed method is called MMF for short because it based on multiscale mean filtering.

1) *Projection and Multiscale Mean Filtering*: The projection profile of the annular panel region, $S(y)$, is calculated by

$$S(y) = \frac{1}{l(y)} \sum_{x=1}^{l(y)} I_{AP}(x, y) \quad (5)$$

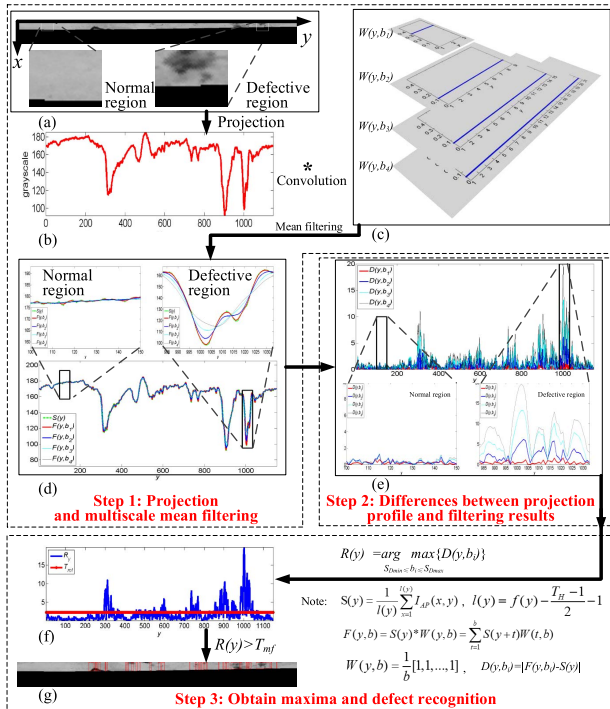


Fig. 8. Flowchart of defect detection for the annular panel region. (a) Annular panel region $I_{AP}(x, y)$, where the white rectangular regions in the left and right of the image are normal and defective regions, respectively. (b) Projection profile $S(y)$. (c) Mean filtering masks with different scales $W(y, b_i)$. (d) Mean filtering results with different scale masks $F(y, b_i)$. (e) $D(y, b_i)$, the differences between $S(y)$ and $F(y, b_i)$. (f) $R(y)$, the maxima of the mean filtering results with multiscale masks. (g) Defect detection result in the annular panel region.

where $I_{AP}(x, y)$ denotes the annular panel region subimage and $l(y)$ is computed by

$$l(y) = f(y) - \frac{T_H - 1}{2} - 1 \quad (6)$$

where T_H denotes the height of the average template and it is an odd number. The input annular panel region is illustrated in Fig. 8(a), the corresponding 1-D signal projection profile $S(y)$, as shown in Fig. 8(b), has considerable noise, and the grayscale values of defects and background often change remarkably in different locations. In addition, defects always clearly appear in the local region. The sizes of defects are generally very small compared with that of the background. To suppress noise, $S(y)$ is fed into the mean filtering as

$$F(y, b) = S(y) * W(y, b) = \sum_{t=1}^b S(y+t)W(t, b) \quad (7)$$

where “*” denotes the convolution operation, and $W(y, b)$ is a general mean filter mask with one row and b columns, that

is,

$$W(y, b) = \frac{1}{b}[1, 1, \dots, 1] \quad (8)$$

with the mask width b as the scale parameter, i.e., the scales and mask widths are one-to-one correspondence.

2) *Differences Between Projection Profile and Filtering Results:* We make defects more noticeable by calculating

$$D(y, b) = |F(y, b) - S(y)|. \quad (9)$$

3) *Obtain Maxima and Defect Recognition:* To make defects with different sizes more noticeable, we set b with different values and calculate the maximum response under all these scales, i.e., $b = \{b_1, b_2, \dots, b_K\}$, K denotes the number of different scales of the filter mask, whose value is empirically configured. The values of b are set evenly between S_{Dmin} and S_{Dmax} , which are the minimal and maximal scales of all possible defects, respectively. They satisfy the requirement that $b_{k+1} - b_k = (S_{Dmax} - S_{Dmin})/(K - 1)$, $b_1 = S_{Dmin}$, and $b_K = S_{Dmax}$, where S_{Dmin} and S_{Dmax} are set by the prior knowledge of defects. We compute the final result by

$$R(y) = \arg \max_{S_{Dmin} \leq b_i \leq S_{Dmax}} \{D(y, b_i)\}. \quad (10)$$

For example, when we set $K = 4$, $S_{Dmin} = 3$, and $S_{Dmax} = 21$. The widths of the mask are $b_1 = 3$, $b_2 = 9$, $b_3 = 15$, and $b_4 = 21$, the masks with different scales are shown in Fig. 8(c).

For the defective and normal regions, the mean filtering results obtained by different scale filters are quite different, as shown in Fig. 8(d). Similarly, $R(y)$ generally has a large value at the defective region. Conversely, the values of $R(y)$ are especially small in the normal region, as revealed in Fig. 8(e). Hence, the maxima of filtering results with different scales are selected for distinguishing the normal and defective regions, as shown in Fig. 8(f). Finally, the parts with $R(y) > T_{mf}$ are regarded as the desired defective regions, as shown in Fig. 8(g).

D. Defect Detection in Central Panel Region

Many foreign objects may exist in the central panel region. The sizes and shapes of foreign objects are distinct from each other, and the position is unknown. Fortunately, there is a common property in that they often cover a small closed area with a local homogeneous gray-level distinct from most of the background region. Meanwhile, defects are typically considered as rare phenomena compared with normal regions. Hence, defective regions will potentially attract the visual attention of the surveyor [48]. Based on this, we proposed two new saliency detection methods for detecting defects in the central panel region. One method, named region growing geodesic saliency (RGGS), is an improved geodesic saliency detection algorithm that combines a redefined region growing algorithm with geodesic distance transform. The other, called

$$R(x, y) = \frac{(I_{AT}(i+x, j+y) - \bar{I}_{AT}(x, y))(T(i, j) - \bar{T})}{\sqrt{\sum_{i=1}^{T_H} \sum_{j=1}^{T_W} (I_{AT}(i+x, j+y) - \bar{I}_{AT}(x, y))^2 \sum_{i=1}^{T_H} \sum_{j=1}^{T_W} (T(i, j) - \bar{T})^2}} \quad (2)$$

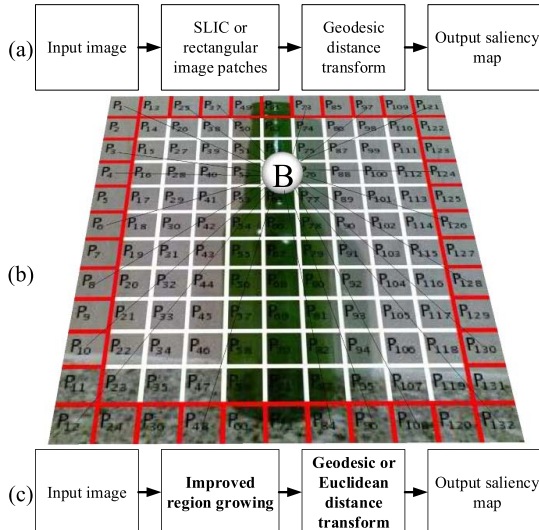


Fig. 9. Pipelines of the original geodesic saliency detection and our improved method. (a) Original geodesic saliency detection algorithm. (b) Undirected weighted graph structure of the original geodesic saliency detection. (c) Our improved method.

region growing Euclidean saliency (RGES), replaces the geodesic distance with Euclidean distance to further accelerate the former.

In the original geodesic saliency detection algorithm [49], the flowchart is mainly composed of two steps: obtaining patches by simple linear iterative clustering (SLIC) [50] or rectangular image patches and computing the saliency value by the geodesic distance transform, as shown in Fig. 9(a), which is usually used for salient object segmentation in color images. The basic idea of the geodesic distance transform with rectangular patches is given as follows. For an image, an undirected weighted graph is constructed, $G = \{V, E\}$. The vertices contain all image patches $\{P_i\}$ and a virtual background node B, $V = \{P_i\} \cup \{B\}$. There are two types of edges: internal edges that connect all adjacent internal patches and boundary edges that connect image boundary patches to the background node. $E = \{(P_i, P_j) | P_i \text{ is adjacent to } P_j\} \cup \{(P_i, B) | P_i \text{ is on the image boundary}\}$, as shown in Fig. 9(b), where the green bottle in the center of the image is the salient object that needs to be extracted. Patches with red and white boundaries are boundary and internal patches, respectively. The white sphere denotes the virtual background node B, which is connected to all boundary patches. The geodesic saliency of a patch P is the accumulated edge weights along the shortest path from P to background node B on the graph G

$$S(P) = \min \sum_{i=1}^{n-1} d(P'_i, P'_{i+1}) \quad (11)$$

such that $P'_i \in \{P_i\}$, $(P'_i, P'_{i+1}) \in \{E\}$ and consider that $P'_1 = P$, P'_n is just B, and P'_i is adjacent to P'_{i+1} .

Wei *et al.* [49] presented two different methods, including rectangular image patches of 10×10 pixels and irregular superpixels obtained by the SLIC algorithm [50] as image patches in order to obtain image patches. The former named GS_GD is faster, and the latter called GS_SP is more accurate.

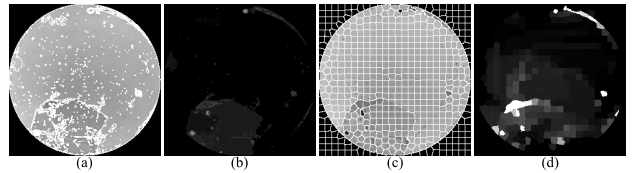


Fig. 10. Demonstration of the RGGS and GS_SP methods. (a) Superpixels obtained by the improved method. (b) Saliency map of RGGS. (c) Superpixels obtained by SLIC method. (d) Saliency map of GS_SP.

GS_SP is quite insensitive to the superpixel algorithm. Thus, any faster superpixel segmentation method can be used [49].

In this paper, we redefined the original geodesic saliency method GS_SP in three aspects to make this method more suitable for defect detection. First, we replaced the SLIC algorithm with an improved region growing algorithm. Second, we redefined that the vertices only contain two types of patches: many undetermined nodes and a determined background node. The latter corresponds to the normal region, which generally has the maximum area in a bottle bottom image. To intuitively show the difference between the RGGS and GS_SP, an example is given in Fig. 10, it is obvious that the proposed RGGS algorithm can obtain more complete background and clearer edge than the existing GS_SP algorithm. Finally, to further speed up the improved method, RGGS, we use the Euclidean distance transformation instead of the geodesic distance transform. The flowchart of our improved method is given in Fig. 9(c). The process of the RGGS- and RGES-based defect detection methods for the central panel region is shown in Fig. 11, it is mainly composed of three steps: obtain image patches, obtain background node, and estimate saliency value and defect recognition.

1) *Obtain Image Patches:* To obtain image patches, we propose a new region growing method that combines region growing with edge detection. First, the input image is fed into the Canny edge detection algorithm. Because the defective region is generally a small closed area, we employ the Douglas–Peucker algorithm [51], [52] to fit the Canny edges to obtain connected curves or closed polygons. The closed polygons and connected curves in the original image are fused. For the fusion image, each curve or polygon is labeled with a unique label. Then, the remaining unlabeled pixels are assigned additional category labels by region growing. We use Euclidean distance to measure the similarity between the seed and the corresponding four-neighbor pixels. The seed is sequentially chosen from the unlabeled regions. The growing process is repeated when the similarity is lower than a threshold T_{rg} , until all remaining adjacent pixels cannot satisfy the condition. The last step is repeated until all pixels have been assigned a label.

To segment the defects as accurately as possible, we implement the region growing process two times and merge the patches whose sizes are lower than a certain threshold into the larger adjacent patch with the most similar gray level. The entire process of this idea is illustrated in Fig. 11(a)–(e).

2) *Obtain Background Node:* For the traditional geodesic saliency detection, background nodes are obtained according to two priors, which are called boundary and connectivity

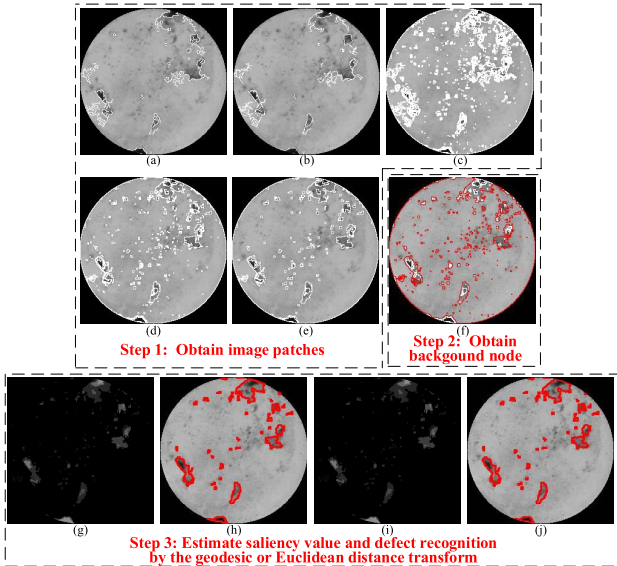


Fig. 11. Process of defect detection in the central panel region. (a) Canny edges. (b) Polygons. (c) Region growing. (d) Region growing iteration. (e) Small area fusion. (f) Background node. The patch with red boundaries is the determined background node whose area is a maximum, and the other patches with red and white boundaries are undetermined nodes. (g) RGGS. (h) Defects obtained by RGGS map. (i) RGES. (j) Defects obtained by RGES map.

priors [49]. The former prior indicates that the image boundary is mostly background. The latter prior indicates that background regions are generally large and homogeneous. However, in this paper, we use only the connectivity prior because defects may appear on the boundary. The image patch whose size is the largest one is taken as the determined background node. $\{P_i\}$ is an image patch, and assume that P_B denotes the determined background node. P_B belongs to $\{P_i\}$

$$|P_B| = \max\{|P_i|\} \quad (12)$$

where $|P_B|$ and $|P_i|$ denote the areas of P_B and P_i , respectively. The central panel region, as shown in Fig. 6(b), is taken as an example, the patches obtained by the proposed method are shown in Fig. 11(f).

3) *Estimate Saliency Value and Defect Recognition*: Consider that the distance between the defective region and the normal region is relatively large. In contrast to the original geodesic saliency, the geodesic saliency value is the length of the shortest path to a virtual background node. In this paper, we take the length of the shortest path to the determined background node P_B as the geodesic saliency value

$$S(P) = \min \left(\sum_{i=1}^{n-2} (P'_i, P'_{i+1}) + d(P'_{n-1}, P_B) \right) \quad (13)$$

such that $P'_i \in \{P_i\}$, $(P'_i, P'_{i+1}) \in \{E\}$. Consider that $P'_1 = P$, and P'_i is adjacent to P'_{i+1} . $S(P)$ and $d(P'_i, P'_{i+1})$ denote the saliency value of the node P and the Euclidean distance between both adjacent nodes P'_i and P'_{i+1} , respectively. Note that we calculate the shortest paths of all image patches by Dijkstra's algorithm [53] for better accuracy.



Fig. 12. Developed visual inspection machine for bottle bottom inspection. (a) Front view of the real system. (b) Side view of the real system.

To further accelerate the proposed saliency detection, we compute the Euclidean distance between the undetermined nodes and the determined background node rather than calculating the geodesic distance between the undetermined nodes and the determined background node, i.e., the saliency value of P_i can be given as

$$S(P_i) = d(P_i, P_B). \quad (14)$$

The saliency maps of RGGS and RGES are presented in Fig. 11(g) and (i), respectively. It is obvious that the saliency values of the defective regions are typically clearly greater than those of normal areas. Thus, a simple threshold method is sufficient to extract defects. In this paper, we define that those regions whose saliency values and areas are greater than the thresholds T_{sm} and T_{area} , respectively, are taken as the real defects. The final results obtained by utilizing the defect recognition rules on the RGGS and RGES saliency maps are shown in Fig. 11(h) and (j), respectively.

IV. EXPERIMENTS

In this section, the defect detection algorithms are tested on bottle bottom images whose resolution and gray levels are 648×483 and 256. First, we construct three glass bottle bottom databases for our statistical analysis. All images in these databases are acquired with our apparatus. The photograph of our developed system is shown in Fig. 12. The first database including 253 normal images and 977 typical defect images is applied to validate our framework, where there are 372, 602, and 702 defect-free region subimages of the central panel, annular panel, and annular texture region, respectively. The second database including the 29 bottle bottom images is used for methods comparison and parameter sensitivity analysis. The other database including 11 images, which are selected from the 29 bottle bottom images, is used to analyze the performance of the localization method. Then, experiments are performed on these three data sets for evaluating the parameter sensitivity and performances of the ROI localization and defect detection. Experiments are conducted on a computer equipped with an Intel(R) Core(TM) i5-4210U (1.7–2.4 GHz) and 6 GB of memory. The program is implemented in Visual C++. The original images and all experimental results are available.¹

¹<https://pan.baidu.com/s/1AUesUSinEq8N2C0O5zaY8w>, download code: 4mq8

A. Measures

To evaluate the performance of the proposed localization method, the center deviation E_X , E_Y , and radius mismatch E_R are defined as

$$E_X = |X_F - X_M| \quad (15)$$

$$E_Y = |Y_F - Y_M| \quad (16)$$

$$E_R = |R_F - R_M| \quad (17)$$

where X_M , Y_M , and R_M are obtained by manual calibration, while X_F , Y_F , and R_F are the results of the localization algorithm. $| * |$ denotes the absolute operation.

To evaluate the defect detection performance, we apply five other measures, including precision (P_r), recall (R_e), F-Measure (F_β), accuracy (A_c), and false detection rate (F_d), which are, respectively, given as

$$P_r = \frac{TP}{TP + FP} \quad (18)$$

$$R_e = \frac{TP}{TP + FN} \quad (19)$$

$$F_\beta = \frac{(1 + \beta^2) P_r R_e}{\beta^2 P_r + R_e} \quad (20)$$

$$A_c = \frac{TP + TN}{TP + TN + FP + FN} \quad (21)$$

$$F_d = \frac{FP}{TP + TN + FP + FN} \quad (22)$$

where true positive (TP), true negative (TN), false positive (FP), and false negative (FN) correspond to the counts of defective unqualified, defect-free qualified, defect-free unqualified, and defective qualified, respectively. β is a weight parameter for P_r and R_e . It is set to one in this paper. A_c is the proportion of correct inspection results. P_r and R_e denote the rates of the correctly detected unqualified products in the total defective and unqualified bottoms, respectively. Except the last measure, F_d , the larger the values of these measures are, the better is the performance of the method.

B. Parameter Sensitivity Analysis

The proposed framework mainly includes five key parameters: T_{rg} , T_{sm} , T_{area} , T_{cc} , and T_{mf} . The first three ones belong to the RGGS- and RGES-based defect detection methods, whereas T_{cc} and T_{mf} belong to the TM- and MMF-based defect detection methods for the annular texture and annular panel regions, respectively. Consider that we adopt different algorithms on three measurement regions, the parameter sensitivity is calculated on the separate measurement region before fusion. All parameters except T_{rg} are selected by maximizing their corresponding F_β . When the value of one parameter is chosen from a range, those of the others remain unchanged. A total of 29 images whose defective regions have been marked manually are used for analyzing the sensitivity of the parameters. Measures are calculated by taking each defective region as the basic unit. In the following, we successively analyze the sensitivities of T_{cc} of TM, T_{mf} of MMF, and T_{rg} , T_{sm} , and T_{area} of RGES.

To verify the sensitivities of T_{mf} and T_{cc} , the values of P_r , R_e , and F_β are calculated on the annular panel and texture

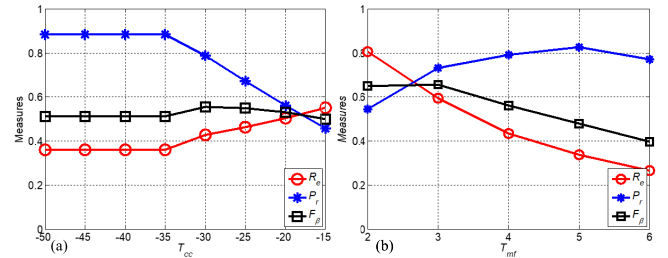


Fig. 13. Measures when T_{cc} and T_{mf} change. (a) Curves of P_r , R_e , and F_β when T_{cc} varies from -50 to -15 with step 5. (b) Curves of P_r , R_e , and F_β when T_{mf} varies from 2 to 6 with step 1.

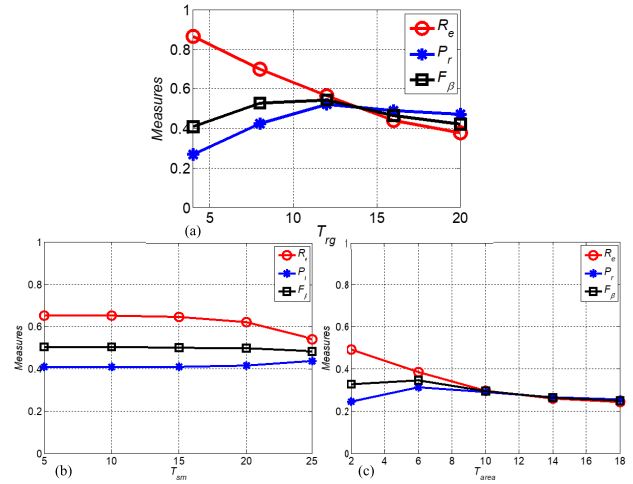


Fig. 14. Measures when T_{rg} , T_{sm} , and T_{area} change. (a) Curves of P_r , R_e , and F_β when T_{rg} ranges from 4 to 20 with step 4. (b) Curves of P_r , R_e , and F_β when T_{sm} ranges from 5 to 25 with step 5. (c) Curves of P_r , R_e , and F_β when T_{area} ranges from 2 to 18 with step 4.

regions of 29 testing images, respectively. As shown in Fig. 13, it is clear that when T_{mf} and T_{cc} are set to the proper values, the corresponding values of F_β can achieve the greatest ones values, i.e., $T_{mf} = 3$ and $T_{cc} = -30$.

To verify the sensitivities of T_{rg} , T_{sm} , and T_{area} , the values of all measures are computed on the central panel region of 29 testing images, and the results are given in Fig. 14. T_{rg} is the only parameter in the process of obtaining patches for the panel region. A good parameter setting of T_{rg} can ensure that the defective regions are divided singly as much as possible, while R_e can measure this ability. Hence, we use R_e to verify the performance of the region growing for defect detection. R_e is inversely proportional to T_{rg} . It is a sensible decision that we set $T_{rg} = 4$ for all cases. T_{sm} and T_{area} are parameters of defect recognition in the central panel region. The larger the values of T_{sm} and T_{area} are, the smaller is the value of R_e . These phenomena occur because the saliency values and area values of the defective region are typically larger than the corresponding thresholds.

C. Method Validation

To evaluate the performance of our framework on the entire bottle bottom, the first data sets including 1230 bottle bottom images in total are used for testing. The key parameters are

TABLE I

QUANTITATIVE INDICES OF THE PROPOSED FRAMEWORK FOR DEFECT DETECTION. THE BOLDED VALUES DENOTE THE BEST RESULTS

Measure	Annular texture	Annular panel	Central panel	total
P_r (%)	77.78	85.60	92.72	92.43
R_e (%)	65.76	61.93	84.62	84.95
F_β (%)	71.27	71.87	88.48	88.53
A_c (%)	72.93	79.19	84.63	82.52
F_d (%)	9.59	4.47	4.63	5.53

TABLE II

PARAMETER SETTINGS OF OUR FRAMEWORK FOR DETECTING DEFECTS OF THREE DIFFERENT TYPES OF BOTTLE BOTTOMS

testing image	T_{cc}	T_{mf}	T_{rg}	T_{sm}	T_{area}
(a)	-35	3	4	10	4
(b)	-35	12	16	30	6
(c)	-30	4	4	10	4

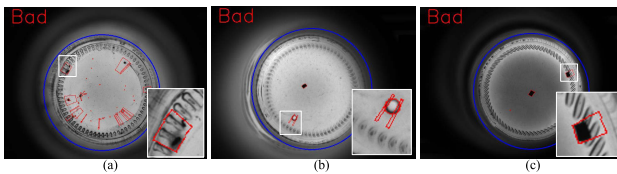


Fig. 15. Defect detection results of three different types of bottle bottoms.

configured as $T_{cc} = -35$, $T_{mf} = 12$, $T_{rg} = 16$, $T_{sm} = 30$, and $T_{area} = 6$. The defect detection performances are verified using the obtained data, the quantitative indices are listed in Table I. Obviously, the false detection rate appears low on all the bottom regions. An exception is with the annular texture region, where the F_d index takes a comparatively high value due to the complex background and structures. Generally, the proposed framework performs well on the good bottle samples with a moderately low over inspection rate (i.e., F_d). Moreover, the total precision and false detection rate are almost equal to the corresponding best results of these three measurement regions. This phenomenon may occur because for the final results, the FP errors increase if the tested bottle bottom is qualified, while the FN errors are accumulated when the defects are in only one region of the three regions. Otherwise, the errors are eliminated.

To validate the conclusion that the proposed framework can be used for many types of bottle bottoms, we test our framework with three different types of bottle bottoms, which have large differences in the texture structure. The parameter settings are given in Table II. Defect detection results are given in Fig. 15. It is obvious that defects in the three bottom images can be detected accurately by changing parameter settings, although the types of bottle bottoms are different.

D. Quantitative Analysis and Comparison

There are four parts addressing the overall bottom inspection issue. Some steps of the proposed pipeline can be replaced with other methods. In this section, we compare the methods of the proposed framework with other existing approaches, but only on separate steps. For the panel regions, we compare

our methods with AD [34], GTS [54], and ATS [54]. For the texture region, we compare the proposed template-matching-based method (TM) with the DFT-based method [24]. A brief introduction about these comparison methods is given as follows.

- 1) *AD*: He *et al.* [34] presented an inverse P–M diffusion model for rail surface defect image enhancement inspired by Tsai's method [32]. It is mainly composed of four steps: nonlinear diffusion, difference operation, threshold binarization, and noise removal. There are three parameters: k , λ , and N_{iter} , where k is a constant and acts as an edge strength threshold, λ is a weighting parameter and N_{iter} denotes the number of iterations. Consider that the features of a rail surface image are similar to those of the panel region of bottle bottom image, we compare AD with our method.
- 2) *GTS and ATS*: Image thresholding enjoys a central position in all types of image segmentation applications because of its implementation simplicity and computational speed [54]. Basic global thresholding and adaptive thresholding using Otsu's method [55] are two of the most popular thresholding methods. The former has only one parameter T_{GTS} , which needs to be set manually. The latter is parameter-free. They have been applied to abstract features or to acquire the connected domain for detecting bottle bottom defects [4], [25]. In this paper, the central panel region of the bottle bottom image is first divided into many parts by thresholding. Then, connected domain analysis is employed on the segmentation results to obtain all suspected defects. Finally, the desired defects are distinguished according to the area and grayscale values of each connected region.
- 3) *DFT*: DFT is the most important discrete transform used to perform Fourier analysis in many practical applications [56]. It converts a finite sequence of equally spaced samples of a function into the same-length sequence of equally spaced samples of the discrete-time Fourier transform. Some researchers have found that there is a definite relationship between the regularity of texture and the Fourier spectrum. In addition, the 2-D DFT can be used to remove the regular texturing of a bottle bottom image [24]. The DFT-based method mainly consists of four parts: DFT, low-pass filtering in the frequency domain, inverse DFT, and ATS. It is also a parameter-free method.

To compare the performance of the above conventional approaches and our methods, first, we accurately mark all defective regions for 29 tested bottle bottom images, which are sufficient to evaluate the performances of methods because there are up to 458, 341, and 147 defective areas in the central panel, annular panel, and annular texture regions, respectively. Second, we calculate the precision, recall, and F-Measure by taking each detected defective region and the true defective region as the basic unit. Moreover, we obtain the time consumption (T_{cs}) of each comparison approach.

- 1) *Circle Detection for ROI Localization*: To analyze the performance of the ROI location method, the boundaries of

TABLE III

ERRORS OF THE LOCALIZATION RESULTS OF THE 11 TESTING IMAGES BY THE PROPOSED LOCATION METHOD. THE 13th ROW MARKED AS “MEAN” IS THE AVERAGE VALUE OF THE CORRESPONDING RESULT

testing image	E_X	E_Y	E_R	$T_{cs}(ms)$
1	2.5	3.5	8.30	43.64
2	2.5	1.5	1.31	45.76
3	1.5	5.5	8.44	47.15
4	2.5	5.5	0.74	48.70
5	3.5	2.5	1.73	51.19
6	0.5	0.5	2.38	41.35
7	6.5	0.5	6.35	55.63
8	3.5	4.5	1.73	50.39
9	3.5	3.5	4.32	36.96
10	2.5	4.5	4.69	51.70
11	0.5	1.5	3.35	47.57
mean	2.68	3.05	3.94	47.28

ROI regions of 11 bottle bottom images are first marked manually. Then, the center and radius, which are denoted by X_M , Y_M , and R_M , respectively, are obtained by the traditional Hough transform circle detection algorithm [45].

Finally, the 21HT algorithm is verified on the 11 calibrated images. The errors of the localization results are shown in Table III. The mean value of E_X is slightly lower than that of E_Y because the testing bottle is clamped by two conveyors, as shown in Fig. 1(a), which can suppress the bottle shifting in the x -direction. The average value of E_R is also small, lower than four pixels, because the difference in size between the two bottles that belong to the same bottle type is very small. In addition, the size is fixed and cannot be affected by additional factors.

2) Annular Texture Region Defect Detection and Analysis:

a) *Parameters setting and testing results:* For each method, we employ a parameter setting method that is similar to parameter sensitivity analysis to evaluate the performance and set the optimal parameters. For TM, we set $T_{cc} = -30$. 29 annular texture subimages are the inputs to TM and DFT for testing. The statistical results and some typical visual results are shown in Table IV and Fig. 16, respectively.

b) *Results analysis:* As shown in Table IV, we can easily find that the comprehensive performance of TM is better than that of DFT. In Fig. 16, we can also discover that small size low-contrast defects locating at the boundary of the texture region can be detected by the proposed TM method, as shown in Fig. 16(b), whereas DFT cannot detect these defects. When a defect with a small size exists in the center of the texture region, it is difficult to be detected correctly by TM and DFT, as shown in Fig. 16(c) and (d). This is a drawback of the two methods. Note that the values of P_r , R_e , and F_β of these methods are not very high because there are many disputed regions that are falsely marked by the normal or defective flag, for instance, even many large and low-contrast defects may also be falsely marked, as shown in Fig. 16(c) and (d). However, these values still have some reference significance for comparing different methods.

3) Annular Panel Region Defect Detection and Analysis:

a) *Parameters setting and testing results:* For MMF and GTS, we set $T_{mf} = 2.3$ and $T_{GTS} = 140$. For AD,

TABLE IV

QUANTITATIVE INDICES FOR DEFECT DETECTION IN THE ANNULAR TEXTURE REGION. NOTE THAT WE TAKE EACH TESTING SUBIMAGE AS A BASIC UNIT TO COMPUTE THE MEASURE A_c . FOR EXAMPLE, FOR TM, $A_c = 27/29$ DENOTES THAT 27 SUBIMAGES ARE CORRECTLY DETECTED. THE BOLDED VALUES DENOTE THE BEST RESULTS

method	$P_r(\%)$	$R_e(\%)$	$F_\beta(\%)$	A_c	$T_{cs}(ms)$
TM	88.83	36.05	51.21	27/29	13.74
DFT	80.95	34.69	48.57	21/29	23.50

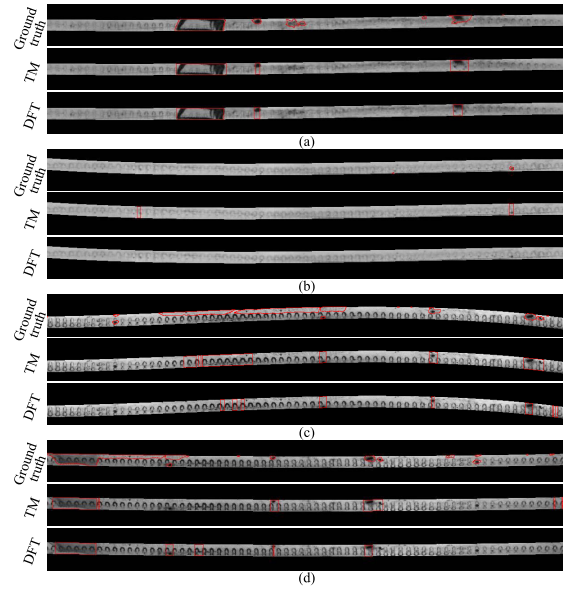


Fig. 16. Visual comparison results of defect detection in the annular texture region using different methods. (a)–(d) Defect detection results for the annular texture region of four bottom images. The first to third rows of each figure are the ground truth, the results of TM and DFT, respectively.

TABLE V
QUANTITATIVE INDICES FOR DEFECT DETECTION IN THE ANNULAR PANEL REGION

method	$P_r(\%)$	$R_e(\%)$	$F_\beta(\%)$	A_c	$T_{cs}(ms)$
MMF	75.95	62.21	68.34	29/29	1.63
AD	20.72	43.99	28.17	29/29	8.51
ATS	39.37	18.43	25.15	19/29	2.57
GTS	45.83	35.48	40.00	16/29	1.70

$k = 100$, $\lambda = 1/2$, and $N_{\text{iter}} = 2$. 29 annular panel subimages are used as inputs of four comparison methods for testing. The statistical results and typical visual results are shown in Table V and Fig. 17, respectively.

b) *Results analysis:* As observed in Table V, it is clear that MMF can achieve the best performance compared with the other three methods in terms of precision, recall, F-Measure, and accuracy. Moreover, MMF is also the fastest method among the compared approaches. The main advantage is that many low-contrast defects can be detected by the proposed MMF because the contrast between saliency regions and the background region was enhanced by the multiscale mean filtering algorithm.

4) Central Panel Region Defect Detection and Analysis:

a) *Parameter settings and testing results:* For RGGS, parameter settings are $T_{rg} = 4$, $T_{sm} = 10$, and $T_{area} = 6$.

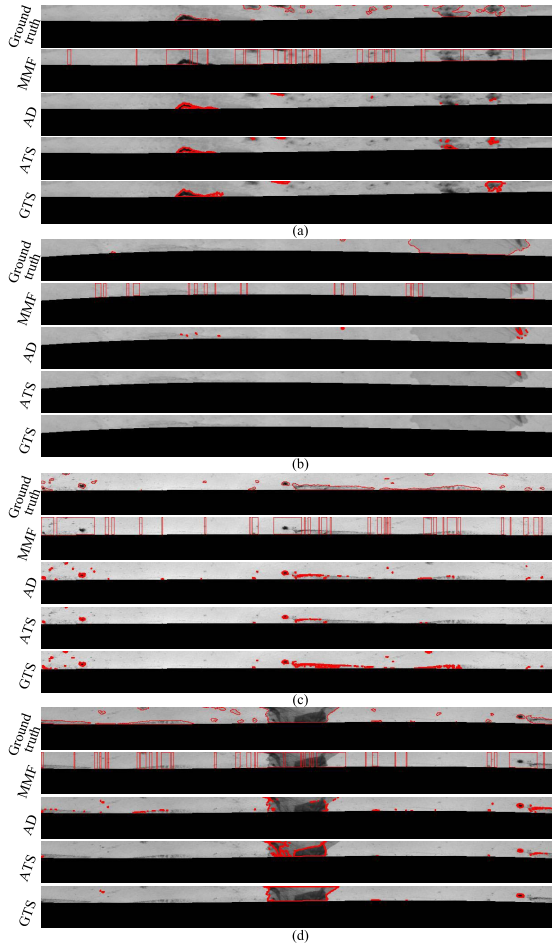


Fig. 17. Visual comparison results of defect detection in the annular panel region using different methods. (a)–(d) Defect detection results for the annular panel region of four bottom images. The first to sixth rows of each figure are the ground truth, the results of MMF, AD, ATS, and GTS, respectively.

TABLE VI
QUANTITATIVE INDICES FOR DEFECT DETECTION IN
THE CENTRAL PANEL REGION

method	$P_r(\%)$	$R_e(\%)$	$F_\beta(\%)$	A_c	$T_{cs}(ms)$
RGGS	41.03	65.15	50.35	29/29	70.26
RGES	41.03	65.15	50.35	29/29	61.70
AD	26.73	28.83	27.74	29/29	4.35
ATS	46.67	12.77	20.06	26/29	1.31
GTS	39.52	59.49	47.49	20/29	0.99

For RGES, $T_{area} = 4$, and the other parameters are same as those for RGGS. The parameter settings of AD in this test are the same as the defect detection test in annular panel region. For GTS, $T_{GTS} = 150$. 29 central panel region subimages are used for testing. The statistical results are shown in Table VI, and some typical visual results are presented in Fig. 18.

b) *Results analysis:* The F-Measure, accuracy, and recall of RGES and RGGS have achieved the highest level among the considered methods. Meanwhile, precision has a high level. Furthermore, as observed in Fig. 18, our method has two merits over the comparative approaches: first, the proposed method can detect small and low-contrast defects accurately since we have used the improved saliency detection algorithm

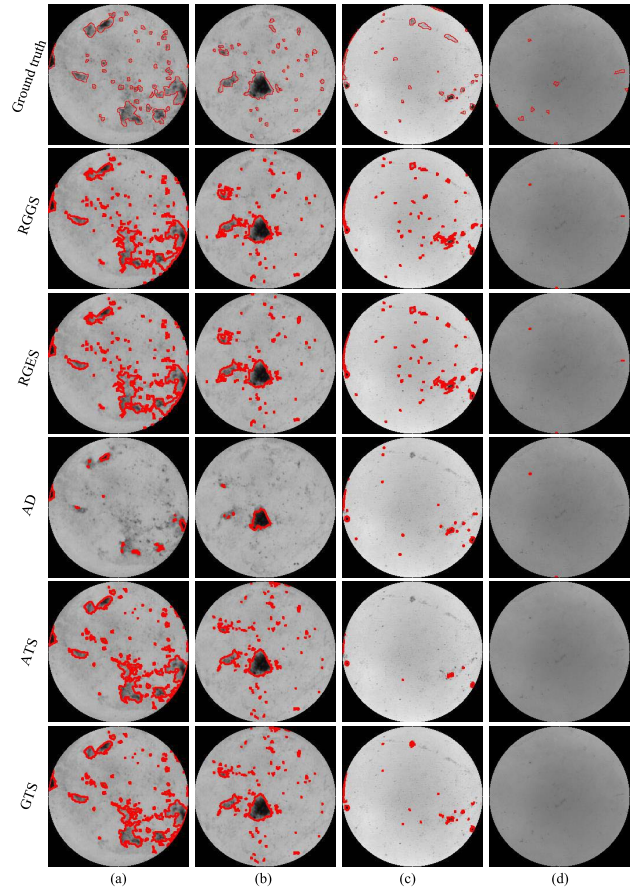


Fig. 18. Visual comparison results of defect detection in the central panel region using different methods. (a)–(d) Defect detection results for the central panel region of four bottom images. The first to sixth rows of each figure are the ground truth, the results of RGGS, RGES, AD, ATS, and GTS, respectively.

to increase the contrast between suspected defects and the background region. Second, the proposed method can obtain accurate boundaries of defective regions, even for those obscure defects, because we have combined region growing with the Canny algorithm, which can precisely detect defect edges.

V. CONCLUSION

In this paper, we have presented a machine vision apparatus for real-time bottle bottom inspection with improved saliency detection and template matching algorithms. First, the bottom is located by 21HT with the shape prior constraint, and it is divided into three parts: central panel region, annular panel region, and annular texture region, for defect detection. Then, separate algorithms are proposed for different measurement regions. We improved the geodesic saliency detection for detecting defects in the central panel region. We employed multiscale mean filtering to inspect defects in the annular panel region. In the annular texture region, we combined template matching with multiscale mean filtering for defect detection. Finally, we used images obtained with our designed system to perform many experiments. The results revealed that the majority of defects with a small size and low contrast can

be inspected correctly. For the three measurement regions, the proposed algorithms can achieve the highest F-Measure, accuracy, and recall while having a high level of precision compared with other methods, where the precision of TM, MMF, and RGES are 88.83%, 75.95%, and 41.03%, respectively. For the first two methods, the precision increased by 7.88% and 30.12%, respectively. The precision of the last method is slightly lower than that of ATS, but the recall, F-measure, and accuracy of RGES are obviously better than those of the other existing methods. Moreover, the proposed methods are robust to pixel value fluctuations. There are still some defects that cannot be correctly detected, particularly defects with a small size in the texture region. In the future, we plan to combine the proposed strategy with machine learning methods to further improve the precision of defect detection.

ACKNOWLEDGMENT

The authors would like to thank Guangzhou VANTA Packing Machinery Technology Company Ltd., Guangdong, China, for their joint development of the inspection machine. They would also like to thank the editors and anonymous reviewers for their help in improving this paper.

REFERENCES

- [1] H. Liu, Y. Wang, and F. Duan, "An empty bottle intelligent inspector based on support vector machines and fuzzy theory," in *Proc. 6th World Congr. Intell. Control Automat.*, Jun. 2006, pp. 9739–9743.
- [2] Y. Yoshino, "Plastic pressure bottle," U.S. Patent 4 254 882 A, Mar. 10, 1981.
- [3] H. Yoshida, "Bottle bottom inspection apparatus," U.S. Patent 4 943 713 A, Jul. 24, 1990.
- [4] F. Duan, Y.-N. Wang, H.-J. Liu, and Y.-G. Li, "A machine vision inspector for beer bottle," *Eng. Appl. Artif. Intell.*, vol. 20, no. 7, pp. 1013–1021, Oct. 2007.
- [5] R. T. Chin and C. A. Harlow, "Automated visual inspection: A survey," *IEEE Trans. Pattern Anal. Mach. Intell.*, vol. PAMI-4, no. 6, pp. 557–573, Nov. 1982.
- [6] Y. Wang, J. Ge, H. Zhang, and B. Zhou, "Intelligent injection liquid particle inspection machine based on two-dimensional Tsallis entropy with modified pulse-coupled neural networks," *Eng. Appl. Artif. Intell.*, vol. 24, no. 4, pp. 625–637, Jun. 2011.
- [7] H. Zhang *et al.*, "Automated machine vision system for liquid particle inspection of pharmaceutical injection," *IEEE Trans. Instrum. Meas.*, vol. 67, no. 6, pp. 1278–1297, Jun. 2018.
- [8] T. Chen, Y. Wang, C. Xiao, and Q. M. J. Wu, "A machine vision apparatus and method for can-end inspection," *IEEE Trans. Instrum. Meas.*, vol. 65, no. 9, pp. 2055–2066, Sep. 2016.
- [9] J. Killings, B. W. Surgenor, and C. K. Mechefske, "A machine vision system for the detection of missing fasteners on steel stampings," *Int. J. Adv. Manuf. Technol.*, vol. 41, nos. 7–8, p. 808, Apr. 2009.
- [10] T. Chen, Y. Wang, and C. Xiao, "An apparatus and method for real-time stacked sheets counting with line-scan cameras," *IEEE Trans. Instrum. Meas.*, vol. 64, no. 7, pp. 1876–1884, Jul. 2015.
- [11] Y. Li, Y. F. Li, Q. L. Wang, D. Xu, and M. Tan, "Measurement and defect detection of the weld bead based on online vision inspection," *IEEE Trans. Instrum. Meas.*, vol. 59, no. 7, pp. 1841–1849, Jul. 2010.
- [12] W. C. Li and D. M. Tsai, "Defect inspection in low-contrast LCD images using Hough transform-based nonstationary line detection," *IEEE Trans. Ind. Informat.*, vol. 7, no. 1, pp. 136–147, Feb. 2011.
- [13] S. Ghosh, A. Mukherjee, M. Gangadaran, and P. K. Dutta, "Automatic defect detection on hot-rolled flat steel products," *IEEE Trans. Instrum. Meas.*, vol. 62, no. 3, pp. 612–621, Mar. 2013.
- [14] C. S. Nandi, B. Tudu, and C. Koley, "A machine vision-based maturity prediction system for sorting of harvested mangoes," *IEEE Trans. Instrum. Meas.*, vol. 63, no. 7, pp. 1722–1730, Jul. 2014.
- [15] R. G. Lins and S. N. Givigi, "Automatic crack detection and measurement based on image analysis," *IEEE Trans. Instrum. Meas.*, vol. 65, no. 3, pp. 583–590, Mar. 2016.
- [16] R. Shanmugamani, M. Sadique, and B. Ramamoorthy, "Detection and classification of surface defects of gun barrels using computer vision and machine learning," *Measurement*, vol. 60, pp. 222–230, Jan. 2015.
- [17] H. Zhang, X. Jin, Q. M. J. Wu, Y. Wang, Z. He, and Y. Yang, "Automatic visual detection system of railway surface defects with curvature filter and improved Gaussian mixture model," *IEEE Trans. Instrum. Meas.*, vol. 67, no. 7, pp. 1593–1608, Jul. 2018.
- [18] L. B. Baldwin, "Device for optimally illuminate bottles for bottom inspection," U.S. Patent 5 436 722 A, Jul. 25, 1995.
- [19] B. L. Hall and L. B. Baldwin, "Machine for inspecting the bottom of glass containers," U.S. Patent, 5 349 435 A Sep. 20, 1994.
- [20] Heuft Corp. (2013). *Heuft Inline Covering Everything: Continuous Empty Bottle Inspection*. [Online]. Available: <https://heuft.com/en/product/beverage/empty-containers/empty-bottle-inspection-heuft-inline>
- [21] Krones Corp. (2016). *The Latest Generation Of Thoroughness: Smart And Reliable Inspection Of Empty Containers*. [Online]. Available: <https://www.krones.com/en/products/machines/linatronic-735-empty-bottle%-inspector.php>
- [22] F. Shafait, S. M. Imran, and S. Klette-Matzat, "Fault detection and localization in empty water bottles through machine vision," in *Proc. E-Tech*, Jul. 2004, pp. 30–34.
- [23] S. Ma, B. Huang, H. Wang, and J. Guo, "Algorithm research on location of bottle mouth and bottom in intelligent empty bottle inspection system," in *Proc. IEEE Int. Conf. Automat. Logistics*, Aug. 2009, pp. 819–824.
- [24] B. Huang, S. Ma, Y. Lv, H. Zhang, C. Liu, and H. Wang, "Research on bottom detection in intelligent empty bottle inspection system," *Indonesian J. Elect. Eng. Comput. Sci.*, vol. 11, no. 10, pp. 5571–5578, Oct. 2013.
- [25] B. Huang *et al.*, "Research and implementation of machine vision technologies for empty bottle inspection systems," *Eng. Sci. Technol. Int. J.*, vol. 21, no. 1, pp. 159–169, Feb. 2018.
- [26] Z. F. Yang and J. Y. Bai, "Vial bottle mouth defect detection based on machine vision," in *Proc. IEEE Int. Conf. Inf. Automat.*, Aug. 2015, pp. 2638–2642.
- [27] W. Zhou, M. Fei, H. Zhou, and K. Li, "A sparse representation based fast detection method for surface defect detection of bottle caps," *Neurocomputing*, vol. 123, pp. 406–414, Jan. 2014.
- [28] X. Li, S. K. Tso, X.-P. Guan, and Q. Huang, "Improving automatic detection of defects in castings by applying wavelet technique," *IEEE Trans. Ind. Electron.*, vol. 53, no. 6, pp. 1927–1934, Dec. 2006.
- [29] H. Y. T. Ngan, G. K. H. Pang, S. P. Yung, and M. K. Ng, "Wavelet based methods on patterned fabric defect detection," *Pattern Recognit.*, vol. 38, no. 4, pp. 559–576, Apr. 2005.
- [30] G. Lambert and F. Bock, "Wavelet methods for texture defect detection," in *Proc. Int. Conf. Image Process.*, Oct. 1997, pp. 201–204.
- [31] S.-M. Chao and D.-M. Tsai, "Anisotropic diffusion with generalized diffusion coefficient function for defect detection in low-contrast surface images," *Pattern Recognit.*, vol. 43, no. 5, pp. 1917–1931, May 2010.
- [32] D.-M. Tsai, C.-C. Chang, and S.-M. Chao, "Micro-crack inspection in heterogeneously textured solar wafers using anisotropic diffusion," *Image Vis. Comput.*, vol. 28, no. 3, pp. 491–501, Mar. 2010.
- [33] S.-M. Chao and D.-M. Tsai, "An anisotropic diffusion-based defect detection for low-contrast glass substrates," *Image Vis. Comput.*, vol. 26, no. 2, pp. 187–200, Feb. 2008.
- [34] Z. He, Y. Wang, F. Yin, and J. Liu, "Surface defect detection for high-speed rails using an inverse P-M diffusion model," *Sensor Rev.*, vol. 36, no. 1, pp. 86–97, Jan. 2016.
- [35] C.-S. Chen, C.-M. Weng, and C.-C. Tseng, "An efficient detection algorithm based on anisotropic diffusion for low-contrast defect," *Int. J. Adv. Manuf. Technol.*, vol. 94, nos. 9–12, pp. 4427–4449, Feb. 2018.
- [36] X. Zhou, Y. Wang, Q. Zhu, C. Xiao, and X. Lu, "SSG: Superpixel segmentation and GrabCut-based salient object segmentation," *Vis. Comput.*, pp. 1–14, Jan. 2018. [Online]. Available: <https://link.springer.com/article/10.1007/s00371-018-1471-4>
- [37] K.-B. Lee, M.-S. Ko, J. J. Lee, T.-M. Koo, and K.-H. Park, "Defect detection method for TFT-LCD panel based on saliency map model," in *Proc. IEEE Region Conf. (TENCON)*, vol. 1, Nov. 2004, pp. 223–226.
- [38] X. Bai, Y. Fang, W. Lin, L. Wang, and B.-F. Ju, "Saliency-based defect detection in industrial images by using phase spectrum," *IEEE Trans. Ind. Informat.*, vol. 10, no. 4, pp. 2135–2145, Nov. 2014.
- [39] Y. Gan and Q. Zhao, "An effective defect inspection method for LCD using active contour model," *IEEE Trans. Instrum. Meas.*, vol. 62, no. 9, pp. 2438–2445, Sep. 2013.

- [40] K. Song and Y. Yan, "Micro surface defect detection method for silicon steel strip based on saliency convex active contour model," *Math. Problems Eng.*, vol. 2013, Nov. 2013, Art. no. 429094, doi: 10.1155/2013/429094.
- [41] L. Tong, W. K. Wong, and C. K. Kwong, *Differential Evolution-Based Optimal Gabor Filter Model for Fabric Inspection*. Amsterdam, The Netherlands: Elsevier, 2016.
- [42] L. Jia, C. Chen, J. Liang, and Z. Hou, "Fabric defect inspection based on lattice segmentation and Gabor filtering," *Neurocomputing*, vol. 238, pp. 84–102, May 2017.
- [43] D. M. Tsai and Y.-C. Hsieh, "Machine vision-based positioning and inspection using expectation–maximization technique," *IEEE Trans. Instrum. Meas.*, vol. 66, no. 11, pp. 2858–2868, Nov. 2017.
- [44] H. K. Yuen, J. Princeen, J. Illingworth, and J. Kittler, "Comparative study of Hough transform methods for circle finding," *Image Vis. Comput.*, vol. 8, no. 1, pp. 71–77, Feb. 1989.
- [45] R. Duda and P. Hart, "Using the Hough transforms to detect lines and curves in pictures," *Commun. ACM*, vol. 15, no. 1, pp. 11–15, 1972.
- [46] X. Zhou, Y. Wang, Q. Zhu, and Z. Miao, "Circular object detection in polar coordinates for 2D LIDAR data," in *Proc. Chin. Conf. Pattern Recognit.*, Nov. 2016, pp. 65–78.
- [47] D. Eberly, R. Gardner, B. Morse, S. Pizer, and C. Scharlach, "Ridges for image analysis," *J. Math. Imag. Vis.*, vol. 4, no. 4, pp. 353–373, Dec. 1994.
- [48] F. Bonnin-Pascual and A. Ortiz, "A probabilistic approach for defect detection based on saliency mechanisms," in *Proc. IEEE Emerg. Technol. Factory Automat. (ETFA)*, Sep. 2014, pp. 1–4.
- [49] Y. Wei, F. Wen, W. Zhu, and J. Sun, *Geodesic Saliency Using Background Priors*. Berlin, Germany: Springer, 2012.
- [50] R. Achanta, A. Shajii, K. Smith, A. Lucchi, P. Fua, and S. Süstrunk, "SLIC superpixels compared to state-of-the-art superpixel methods," *IEEE Trans. Pattern Anal. Mach. Intell.*, vol. 34, no. 11, pp. 2274–2282, Nov. 2012.
- [51] U. Ramer, "An iterative procedure for the polygonal approximation of plane curves," *Comput. Graph. Image Process.*, vol. 1, no. 3, pp. 244–256, Nov. 1972.
- [52] D. H. Douglas and T. K. Peucker, "Algorithms for the reduction of the number of points required to represent a digitized line or its caricature," *Cartographica, Int. J. Geograph. Inf. Geovis.*, vol. 10, no. 2, pp. 112–122, Dec. 1973.
- [53] E. W. Dijkstra, "A note on two problems in connexion with graphs," *Numerische Mathematik*, vol. 1, no. 1, pp. 269–271, Dec. 1959.
- [54] R. C. Gonzalez and R. Woods, *Digital Image Processing*, 3rd ed. Beijing, China: Publishing House Electronics Industry, 2017, pp. 763–769.
- [55] N. Otsu, "A threshold selection method from gray-level histograms," *IEEE Trans. Syst., Man, Cybern.*, vol. SMC-9, no. 1, pp. 62–66, Jan. 1979.
- [56] G. Strang, "Wavelets," *Amer. Sci.*, vol. 82, no. 3, pp. 250–255, 1994.



Xianen Zhou received the B.S. degree from the Hunan University of Science and Engineering, Yongzhou, China, in 2010, and the M.S. degree in circuits and systems from the East China University of Technology, Nanchang, China, in 2013. He is currently pursuing the Ph.D. degree with Hunan University, Changsha, China.

His current research interests include machine vision, machine learning, and automatic visual detection systems.



Yaonan Wang received the B.S. degree in computer engineering from the East China University of Technology, Nanchang, China, in 1981, and the M.S. and Ph.D. degrees in electrical engineering from Hunan University, Changsha, China, in 1990 and 1994, respectively.

From 1998 to 2000, he was a Senior Humboldt Fellow in Germany, and from 2001 to 2004, he was a Visiting Professor with the University of Bremen, Bremen, Germany. Since 1995, he has been a Professor with Hunan University. His current research interests include intelligent control, image processing, and computer vision systems for industrial applications.



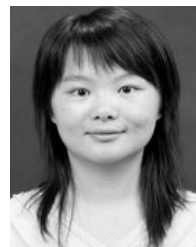
Changyan Xiao received the B.Eng. and M.S. degrees in mechanical and electronic engineering from the National University of Defense Technology, Changsha, China, in 1994 and 1997, respectively, and the Ph.D. degree in biomedical engineering from Shanghai Jiaotong University, Shanghai, China, in 2005.

From 2008 to 2009, he was a Visiting Post-Doctoral Researcher with the Division of Image Processing, Leiden University Medical Center, Leiden, Netherlands. Since 2005, he has been an Associate Professor and a Full Professor with the College of Electrical and Information Engineering, Hunan University, Changsha. His current research interests include medical imaging, machine vision, and embedded instruments.



Qing Zhu received the B.Sc., M.Sc., and Ph.D. degrees in electrical engineering from Hunan University, Changsha, China, in 1989, 2000, and 2008, respectively.

She is currently an Associate Professor and a Ph.D. Supervisor with the College of Electrical and Information Engineering, Hunan University. Her current research interests include voice and image processing and network and communication technology.



Xiao Lu received the B.E. degree in electrical engineering from Hunan University, Changsha, China, in 2007, the M.S. degree in electrical engineering from Southeast University, Nanjing, China, in 2010, and the Ph.D. degree in electrical engineering from Hunan University in 2016.

She is currently an Associate Professor with Hunan Normal University, Changsha. Her current research interests include machine vision, pattern recognition, and machine learning.



Hui Zhang received the B.S., M.S., and Ph.D. degrees in pattern recognition and intelligent system from Hunan University, Changsha, China, in 2004, 2007, and 2012, respectively.

He is currently an Assistant Professor with the College of Electrical and Information Engineering, Changsha University of Science and Technology, Changsha. He is also a Visiting Scholar with the Computer Vision and Sensing System Laboratory, Department of Electrical and Computer Engineering, University of Windsor, Windsor, ON, Canada. His current research interests include machine vision, sparse representation, and visual tracking.



Ji Ge received the B.S. and M.S. degrees in mechatronics engineering from the Jiangxi University of Science and Technology, Ganzhou, China, in 2002 and 2005, respectively, and the Ph.D. degree in pattern recognition and intelligent system from Hunan University, Changsha, China, in 2012.

He is currently a Post-Doctoral Fellow with the Department of Mechanical and Industrial Engineering, University of Toronto, Toronto, ON, Canada. His current research interests include machine learning and computer vision.



Huihuang Zhao received the Ph.D. degree in mechano-electronic engineering from Xidian University, Xi'an, China, in 2010.

From 2013 to 2015, he was a Post-Doctoral Researcher with Hunan University, Changsha, China. From 2016 to 2017, he was an Academic Visitor with the School of Computer Science and Informatics, Cardiff University, Cardiff, U.K., where he has been a Sponsor Researcher with the School of Computer Science and Informatics since 2017. He is currently an Associate Professor with the College of Computer Science and Technology, Hengyang Normal University, Hengyang, China. His current research interests include image processing, compressive sensing, deep learning, and 3-D geometry processing.